ADVANCED ELECTRONIC MATERIALS
www.advelectronicmat.de

Massive Magnetostriction of the Paramagnetic Insulator $KEr(MoO_4)_2$ via a Single-Ion Effect

Bence Bernáth, Khrystyna Kutko, Steffen Wiedmann, Olga Young, Hans Engelkamp, Peter C. M. Christianen, Sergii Poperezhai, Leonid V. Pourovskii, Sergii Khmelevskyi, and Dmytro Kamenskyi**

The magnetostriction phenomenon, which exists in almost all magnetically ordered materials, is proved to have wide application potential in precision machinery, microdisplacement control, robotics, and other high-tech fields. Understanding the microscopic mechanism behind the magnetostrictive properties of magnetically ordered compounds plays an essential role in realizing technological applications and helps the fundamental understanding of magnetism and superconductivity. In paramagnets, however, the magnetostriction is usually significantly smaller because of the magnetic disorder. Here, the observation of a remarkably strong magnetostrictive response of the insulator paramagnet $KEr(MoO_4)_2$ is reported on. Using low-temperature magnetization and dilatometry measurements, in combination with ab initio calculations, employing a quasi-atomic treatment of many-body effects, it is demonstrated that the magnetostriction anomaly in $KEr(MoO_4)_2$ is driven by a single-ion effect. This analysis reveals a strong coupling between the Er^{3+} ions and the crystal lattice due to the peculiar behavior of the magnetic quadrupolar moments of Er^{3+} ions in the applied field, shedding light on the microscopic mechanism behind the massive magnetostrictive response.

1. Introduction

Magnetostriction relates to a lattice deformation of a crystalline solid induced by an applied magnetic field, and is found to be very strong in elementary rare-earth crystals and their alloys, particularly in magnetically ordered compounds (ferro-, antiferromagnets).[1–3] The fundamental understanding of magnetostrictive effects boosted the technological application of these materials; from magnetic shielding to actuators, rare-earth compounds are widely used.[4–7] Despite the robust understanding of magnetostriction in ordered rare-earth compounds,[8] and the growing interest toward rare-earth based paramagnetic compounds that show magnetocaloric[9] and magnetoelectric[10] effects, we know much less about the magnetostrictive response of paramagnetic compounds.[11–16] In contrast to ferro- and

B. Bernáth, S. Wiedmann, O. Young, H. Engelkamp, P. C. M. Christianen, D. Kamenskyi
High Field Magnet Laboratory (HFML - EMFL)
Radboud University
Toernooiveld 7, ED 6525 Nijmegen, The Netherlands
E-mail: bence.bernath@ru.nl

B. Bernáth, S. Wiedmann, O. Young, H. Engelkamp, P. C. M. Christianen, D. Kamenskyi
Radboud University
Institute for Molecules and Materials
Heyendaalseweg 135, AJ 525 Nijmegen, The Netherlands

K. Kutko, S. Poperezhai
B. Verkin Institute for Low Temperature Physics and Engineering of the National Academy of Sciences of Ukraine
Nauky Ave 47, 61103 Kharkiv, Ukraine

The ORCID identification number(s) for the author(s) of this article can be found under https://doi.org/10.1002/aelm.202100770.

DOI: 10.1002/aelm.202100770

L. V. Pourovskii
CPHT
CNRS
Ecole Polytechnique
Institut Polytechnique de Paris
Route de Saclay
91128 Palaiseau, France

L. V. Pourovskii
Collège de France
11 place Marcelin Berthelot, 75005 Paris, France

S. Khmelevskyi
Research Center for Materials Science and Engineering
Vienna University of Technology
Karlsplatz 13, A-1040 Vienna, Austria

D. Kamenskyi
FELIX Laboratory
Radboud University
Toernooiveld 7, ED 6525 Nijmegen, The Netherlands

D. Kamenskyi
Molecular Photoscience Research Center
Kobe University
Kobe 657-8501, Japan

D. Kamenskyi
Experimental Physics V
Center for Electronic Correlations and Magnetism
Institute of Physics
University of Augsburg
86159 Augsburg, Germany
E-mail: dmytro.kamenskyi@physik.uni-augsburg.de

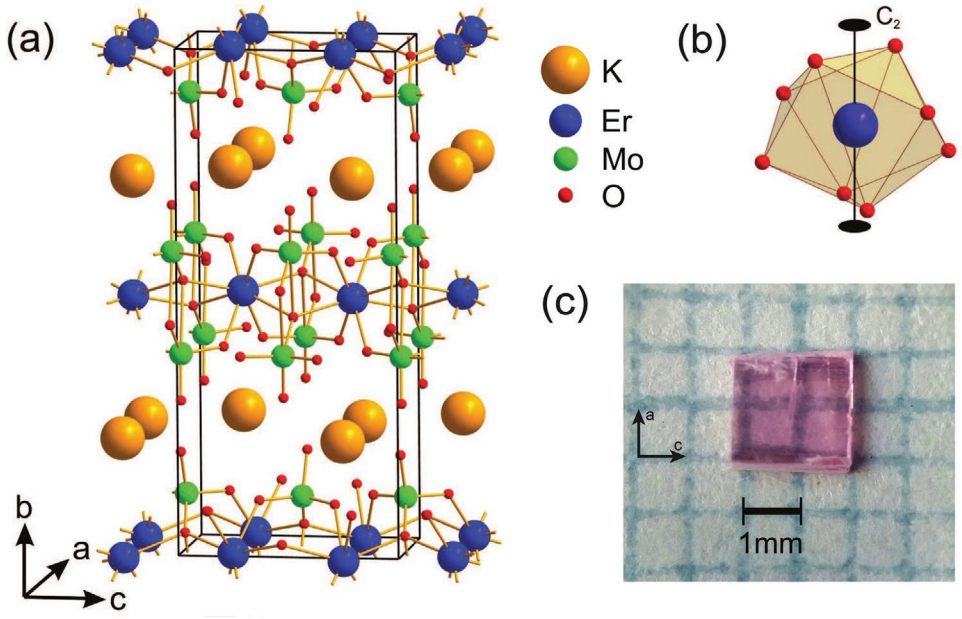

Figure 1. a) Crystallographic structure of $KEr(MoO_4)_2$. b) Local environment of the Er^{3+} ions (blue sphere). c) Photo of the sample used for the experiments.

antiferromagnets, in paramagnets correlations between individual magnetic moments of single ions are much smaller; therefore, there is no magnetic ordering down to very low temperatures (for rare-earth compounds, the ordering temperature often is below 1 K).

While the magnetostrictive behavior in magnetically ordered compounds can be explained by collective phenomena,[1–3] in elementary rare earth compounds and their alloys, the contribution of single-ion spin orbit mechanism plays a key role.[7,8] The single-ion effect or mechanism refers to the complex interaction of magnetic 4*f*-ions with the surrounding crystal lattice, irrespective of inter-ion exchange interaction or correlation effects.[17] However, the bare single-ion effect is notoriously difficult to study. In magnetic materials, it is often obscured by collective phenomena due to the onset of magnetic ordering induced by interactions between ions. Even in compounds where magnetic interactions are frustrated, and the ordering temperature is suppressed down to a few kelvin, the inter-ion correlations remain significant.[18] In some rare-earth based magnetic insulators, the inter-ion exchange interaction can be suppressed markedly due to strong localization of the *f*-orbitals.[19] As a result, these compounds remain in the paramagnetic phase down to sub-Kelvin temperatures where the single-ion effect then emerges. A good example is the family of the rare-earth paramagnetic compounds $KRe(MoO_4)_2$ (*Re* is an rare-earth element). In these systems, the dipole–dipole interaction of about 1 K is the largest interaction between the Re^{3+} ions and magnetic order appears only below 1 K.[20–22] Here, we focus on $KEr(MoO_4)_2$, which exhibits no magnetic order above 0.95 K.[22] The dipole–dipole interaction can be estimated by: $E_{dd}/k_B = \frac{\mu_0 \mu_{Er^{3+}}^2}{4\pi r^3 k_B} \approx 0.8$ K (0.07 meV), where E_{dd} is the energy of the dipole–dipole interaction, k_B is the Boltzmann constant, μ_0 is the permeability of free space, $\mu_{Er^{3+}} = 9\,\mu_B$ is the magnetic moment of an Er^{3+} ion, and r = 3.95 Å is the shortest distance between the nearest erbium ions.[20] In this study, the lowest experimental temperature is 1.3 K; therefore, the effect of the dipole–dipole interaction is negligible.

The crystal structure of rare-earth based insulators, such as $KEr(MoO_4)_2$, is defined by an equilibrium between the elastic energy of the crystal lattice and the ground state multiplet energy of the magnetic ions, here Er^{3+}.[23] **Figure 1**a displays the crystallographic structure of $KEr(MoO_4)_2$ and Figure 1b shows the local environment of the Er^{3+} ion; an oxygen polyhedron with C_2 symmetry axis along the *b*-direction. The environment generates an effective crystal electric field (CEF) on the Er^{3+} sites and lifts the degeneracy of the lowest Er^{3+} multiplet $^4I_{15/2}$. This multiplet then splits into eight Kramers doublets[24,25] and stabilizes an orthorhombic crystal structure with a D_{2h}^{14} (*Pbcn*) space group.[26] A pronounced layered structure of the compound results in plate-shaped transparent single crystals (Figure 1c) with the crystallographic *b* axis perpendicular to the plate. The pink tint of the compound is due to the splitting of the atomic terms of Er^{3+} which falls in the visible range.[24]

Due to the Zeeman effect, an externally applied magnetic field splits the Kramers doublets and shifts the balance between the elastic and electronic energies. In anisotropic *Re*-based materials, the Zeeman splitting of the individual Kramers doublets may exceed 0.6 meV per Tesla (for g-factor above 10). This splitting is very significant, especially when the measured CEF splitting between the lowest levels of the $^4I_{15/2}$ multiplet is about 1.6 meV as it is in $KEr(MoO_4)_2$. Such a small energy scale enables the manipulation of the single-ion energy spectrum (e.g., field-induced level crossing) by applying high, but still accessible magnetic field.[25] $KEr(MoO_4)_2$ offers a great opportunity to study the magnetic field-induced single-ion effect. In addition, on $KEr(MoO_4)_2$, a giant rotational magnetocaloric effect was reported earlier, suggesting a significant application potential for magnetic refrigeration.[9]

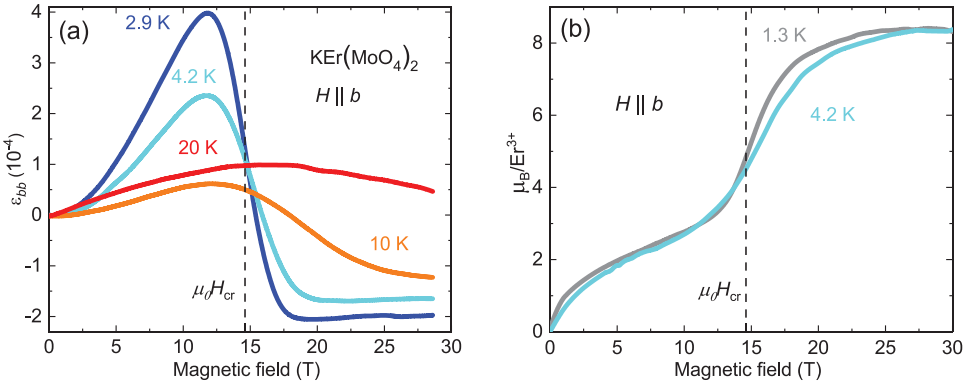

Figure 2. a) Magnetoelastic strain at 2.9, 4.2, 10.0, and 20.0 K. $\varepsilon_{bb} = \Delta l/l$, where $\Delta l = l(H, T) - l(0, T)$. The *bb* subscript indicates that the field has been applied along the *b*-axis and the strain was also measured in this direction. The vertical dashed line locates the critical field, $\mu_0 H_{cr}$. b) Magnetization of $KEr(MoO_4)_2$. Measurements have been performed with the magnetic field applied along the *b*-axis at 1.3 and 4.2 K.

Here, we investigate the magnetostriction of $KEr(MoO_4)_2$ with a magnetic field applied along the *b*-axis, which is the magnetic hard direction.[27] To probe the response of the Er^{3+} ions and the crystal lattice separately, we employ magnetometry and dilatometry, respectively. The magnetic field response of $KEr(MoO_4)_2$ is dictated by Er^{3+} since these are the only magnetic ions in the compound. The coupling between the Er^{3+} ions and the crystal lattice has been evaluated by means of ab initio calculations, which reveal the microscopic mechanism of the observed lattice deformation. Our results indicate that the massive lattice deformation in $KEr(MoO_4)_2$ is due to the single-ion effect. The theory explains this microscopic mechanism with the magnetic field response of the magnetic quadrupolar moment of the Er^{3+} ion.

2. Results and Discussion

2.1. Experimental Observations

We probe the lattice response by a high-resolution capacitance dilatometer for magnetostriction measurements in magnetic fields up to 30 T.[29] **Figure 2**a shows magnetoelastic strain curves taken at 2.9, 4.2, 10.0, and 20.0 K, with magnetic field, $\mu_0 H \| b$. The magnetostriction is expressed by relative units of the magnetoelastic strain, $\varepsilon_{bb} = \Delta l/l$ where l is the initial sample length at $H = 0$ T and $\Delta l = l(H, T) - l(0, T)$ measured along the applied field. The *bb* subscript indicates that the field was applied along the *b*-axis and the strain was also measured in this direction.

Below 10 T, the sample expands along the applied magnetic field, with a more prominent effect at low temperatures, which is the typical magnetostricitve behavior of paramagnets (i.e., parastriction).[13,30] For 12 T $\leqslant \mu_0 H \leqslant$ 17 T, the magnetostriction exhibits an anomaly. When the magnetic field exceeds 12 T, the sample shrinks with very high field sensitivity and saturates above 17 T. At $T = 2.9$ K, the magnetoelastic strain exhibits a peak-to-peak change of $\approx 6 \times 10^{-4}$. Interestingly, such a strong magnetostriction is usually observed in metallic antiferromagnets, for example, $ErNi_2B_2C$, NdB_6 or $ErGa_2$.[8] Rare-earth paramagnetic oxides such as $Tm_3Ga_5O_{12}$ or $Yb_3Al_5O_{12}$ show at least one order of magnitude smaller magnetoelastic strain.[12]

Figure 2b shows the magnetization, M, measured along the applied magnetic field parallel to the *b* axis, $H \| b$. The magnetization measured by a vibrating sample magnetometer[31] at 1.3 and 4.2 K. The vertical dashed lines in Figure 2a,b show the critical field of $\mu_0 H_{cr} = 14.6$ T (determined by the inflection point of the magnetoelastic strain curve at 2.9 K where the thickness of the sample exhibit the highest sensitivity to applied magnetic field) when the magnetostriction and magnetization curves exhibit anomalies.

Table 1. Measured[24,25,36] and calculated energies of the splitting of the $^4I_{15/2}$ multiplet relative to the ground state at $\mu_0 H = 0$ T. The corresponding wavefunctions are shown in Table S2, Supporting Information.

Measured (meV)	1.6	3.9	9.2	21.3	30.9	38.4	39.1
Calculated (meV)	1.6	3.4	7.6	23.2	32.7	44.8	45.9

2.2. Phenomenology and Theory

For the phenomenological description of the magnetostriction in $KEr(MoO_4)_2$, we use the Hamiltonian:

$$\mathcal{H} = \mathcal{H}_Z + \mathcal{H}_E + \mathcal{H}_{ME} + \mathcal{H}_{CEF} \quad (1)$$

where $\mathcal{H}_Z$, $\mathcal{H}_E$, $\mathcal{H}_{ME}$, and $\mathcal{H}_{CEF}$ are the Zeeman, elastic, magnetoelastic, and CEF terms. The Zeeman term reads:

$$\mathcal{H}_Z = \mu_B \mu_0 \mathbf{H}(\mathbf{L} + 2\mathbf{S}) \quad (2)$$

where μ_B is the Bohr magneton, $\mathbf{H}$ is the magnetic field strength, $\mathbf{L}$ and $\mathbf{S}$ are the electronic orbital and spin moments, respectively. The elastic term is given by

$$\mathcal{H}_E = \frac{V_0}{2} \sum_{ij} C_{ij} \varepsilon_i \varepsilon_j \quad (3)$$

where $\varepsilon_{i(j)}$ are the strain tensor components (in Voigt notation), C_{ij} are elastic constants, and V_0 is the unit cell volume per formula unit. Only C_{11}, C_{22}, C_{33}, C_{12}, C_{13}, C_{23}, C_{44}, C_{55}, and C_{66} can be non-zero in an orthorhombic crystal.[32] In orthorombic crystals, using the lowest order of the 4*f*-ion angular momentum

operator, the coupling between the Er^{3+} ions and the crystal lattice is described via the magnetoelastic Hamiltonian:[13,33,34]

$$\begin{aligned}\mathcal{H}_{ME} &= B^1_{10}\varepsilon_{xx}Q_{3z^2} + B^1_{11}\varepsilon_{xx}Q_{x^2-y^2} \\ &+ B^1_{20}\varepsilon_{yy}Q_{3z^2} + B^1_{21}\varepsilon_{yy}Q_{x^2-y^2} \\ &+ B^1_{30}\varepsilon_{zz}Q_{3z^2} + B^1_{31}\varepsilon_{zz}Q_{x^2-y^2} \\ &+ B^2\varepsilon_{xy}Q_{xy} + B^3\varepsilon_{xz}Q_{xz} \\ &+ B^4\varepsilon_{yz}Q_{yz}\end{aligned} \tag{4}$$

where Q_α is the projection α of the quadrupole momentum operator, and B^μ_{jm} are the magnetoelastic coefficients. The local frame is $x\|b$, $y\|c$, and the quantization axis $z\|a$. Note that the dipole magnetic moments of the 4*f* ions, which are proportional to the angular momentum expectation values, appear only in the Zeeman term. In contrast, magnetoelastic interactions only depend on the even powers of the magnetic moment or angular momentum operators.

The CEF splitting of electronic levels is expressed by $\mathcal{H}_{CEF}$ (Stevens operators and their coefficients)[35]:

$$\mathcal{H}_{CEF} = \sum_{kq} A^q_k \left\langle r^k \right\rangle \Theta_k \hat{O}^q_k \tag{5}$$

where the Stevens operator equivalents $\hat{O}^q_k$ act within the Er f^{11} atomic ground-state multiplet $^4I_{15/2}$. $A^q_k\left\langle r^k\right\rangle$ are CEF parameters Θ_k are Stevens factors for k = 2, 4, 6. $A^q_k\left\langle r^k\right\rangle$ dictate the splitting of the $^4I_{15/2}$ multiplet which has been studied previously by means of optical[24] and far-infrared[25,36] spectroscopy. The results of these measurements are summarized in the top row of **Table 1**. The low site symmetry (C_2) of the Er^{3+} ions leads to fifteen $A^q_k\left\langle r^k\right\rangle$ constants in $\mathcal{H}_{CEF}$.[37] A large number of free parameters and a strong lattice distortion that significantly affect the CEF make the fitting of the $A^q_k\left\langle r^k\right\rangle$ constants practically not feasible. Therefore, we have chosen a different approach to explain our experimental observations.

We use a state-of-the-art ab initio methodology[38] based on the density functional and dynamical mean-field theory (DFT+DMFT)[39,40] in conjunction with a quasi-atomic Hubbard-I (HI)[41] approximation of the local correlations of the 4*f* electrons of the Er atom. The self-consistent DFT+HI calculations predict that the CEF splits the $^4I_{15/2}$ atomic multiplet to have the lowest energy, in agreement with Hund's rules for a 4*f* shell; the calculated spin-orbit coupling λ = ~0.27 eV. The predicted CEF splitting of the $^4I_{15/2}$ multiplet is shown in Table 1 bottom row.

The obtained splitting energies of the $^4I_{15/2}$ multiplet are in an exceptionally good quantitative agreement with the spectroscopy results.[24,25,36] The $A^q_k\left\langle r^k\right\rangle$ CEF parameters at zero magnetic field are listed in Table S1, Supporting Information. The first-principle calculations determine the energies of the $^4I_{15/2}$ multiplet splittings, the associated wave-functions, and the CEF parameters (see Supporting Information) based on the room temperature crystallographic structure of $KEr(MoO_4)_2$.[42] Our ab initio calculation provides the field dependence of the magnetic quadrupolar moment operator Q of the Er^{3+} ions involved in the ion-lattice coupling. Thus, it is possible to understand the observed peculiar high-field behaviour of magnetostriction by finding the equilibrium among the different interactions. We consider the total energy as a function of the elastic strain ε_{bb} and the quadrupolar moment $\langle Q_\alpha\rangle_H$, which is the expectation value of the projection α of the quadrupolar moment operator Q at magnetic field H. Due to the low point-group symmetry, the Er quadrupolar moments in $KEr(MoO_4)_2$ are non-zero even at $\mu_0 H$ = 0 T; the magnetostriction is thus induced by the modification of the quadrupolar moments with respect to their zero-field value, $\Delta\langle Q_\alpha\rangle = \langle Q_\alpha\rangle_H - \langle Q_\alpha\rangle_{H=0}$. Taking into account terms along the applied magnetic field ($H\|b$), the total energy reads:

$$E_{\text{tot}} = B^1_{10}\varepsilon_{bb}\Delta\left\langle Q_{3z^2}\right\rangle + B^1_{11}\varepsilon_{bb}\Delta\left\langle Q_{x^2-y^2}\right\rangle + \frac{V_0 C_{bb}\varepsilon^2_{bb}}{2} + \cdots \tag{6}$$

The first and the second terms are the magnetoelastic contributions and the last term is the elastic one; C_{bb} is the corresponding elastic constant(based on Equation (3); C_{bb} represents C_{xx}). The +... stands for other elastic and magnetoelastic terms. A first-principles evaluation of the magnetoelastic constants B_{ij} for the $KEr(MoO_4)_2$ system (48 atoms/unit cell) is not feasible at present since it would require high-precision total-energy DFT+DMFT calculations for multiple very large and distorted cells, which is beyond the current state-of-the-art. For the following semi-quantitative analysis, the contribution of the perpendicular terms to the total energy is neglected, allowing only two independent parameters $\frac{B^1_{11}}{B^1_{10}}$ and $\frac{B^1_{10}}{V_0 C_{bb}}$ to fit an experimental magnetostriction curve. This approximation is justified by the layered structure of $KEr(MoO_4)_2$. As was shown by THz spectroscopy,[36] weak bonding between $[Er(MoO_4)_2]^-$ and K^+ layers along the *b*-axis causes that shear vibrations in the *ac* plane to have exceptionally low energies of 2.1 and 3.2 meV along the *a* – and *c* – axes, respectively. Bonding inside $[Er(MoO_4)_2]^-$ layers is much stronger and the strain ε_{bb} along the *b*-axis is expected to be significantly larger as compared to ε_{aa} and ε_{cc}. Due to the quadratic contribution of the strain (ε_{bb}) to the last term of Equation (6), we neglect the contributions of the ε_{aa} and ε_{cc} despite the elastic constant C_{bb} for the *b*-direction being smaller than C_{aa} and C_{cc}.[43] The value of C_{bb} could be obtained based on the sound velocity of $S_{bb} = 2.93\times10^3$ m s^{-1}.[43] $C_{bb} = \rho\times S^2_{bb} = 41$ GPa, where ρ = 4.78 g cm^{-3}. From the condition of stability of an orthorhombic crystal,[32] $C^2_{ij} < C_{ii}C_{jj}$, one thus infers that the off-diagonal elastic constants C_{ab} and C_{bc} are significantly smaller than C_{bb}. Neglecting those off-diagonal contributions results in decoupling of the terms involving ε_{bb} from the rest, leading to the approximation mentioned above. We adopt below the simplified notation $K \equiv V_0 C_{bb}$ for the only relevant elastic constant.

The equilibrium value of ε_{bb} at given values of the quadrupolars $\left\langle Q_{3z^2}\right\rangle$ and $\left\langle Q_{x^2-y^2}\right\rangle$ is obtained by the minimization of Equation (6), $\frac{\partial E_{\text{tot}}}{\partial\varepsilon_{bb}} = 0$, resulting in the following equation:

$$\varepsilon_{bb} = -\frac{B^1_{10}\Delta\left\langle Q_{3z^2}\right\rangle + B^1_{11}\Delta\left\langle Q_{x^2-y^2}\right\rangle}{K} \tag{7}$$

The quadrupolar moment operators Q_{3z^2} and $Q_{x^2-y^2}$ are defined as

$$Q_{3z^2} = 2J^2_z - J^2_x - J^2_y \tag{8}$$

$$Q_{x^2-y^2} = J^2_x - J^2_y \tag{9}$$

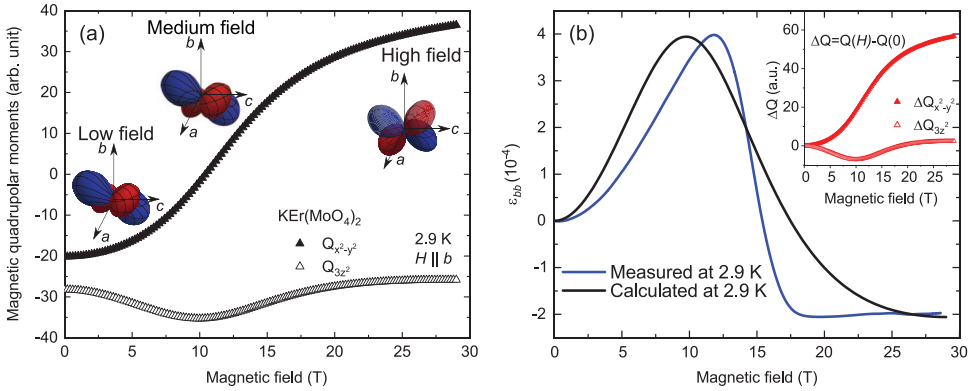

Figure 3. a) Results of the ab initio calculations. Quadrupolar moments are calculated at 2.9 K with the magnetic field along the *b*-axis. The values of the Q_{3z^2} and $Q_{x^2-y^2}$ quadrupolar moments are shown by the empty and filled triangles, respectively. The insets are the visualization of the total quadrupolar moments rotation in magnetic field. They show the absolute-value isosurfaces of the calculated quadrupolar moment and a negative (positive) sign is indicated by a blue (red) color. b) Comparison between the theory and experiment for the magnetostrictive strain. The blue curve is the measured magnetostrictive strain at 2.9 K (the same curve is shown in Figure 2). The black curve is the calculated magnetostrictive strain. The inset shows the $\langle Q_{3z^2} \rangle$ and $\langle Q_{x^2-y^2} \rangle$ values.

where $J_{x,\ y,\ z}$ are the components of the total angular momentum operator. The calculated field dependence of Q_α is shown in **Figure 3**a. The two projections show different behaviors. Whereas the $Q_{x^2-y^2}$ component monotonously increases with field and shows a zero-crossing at a field of about 9 T, the Q_{3z^2} component first decreases down to 10 T, and then increases toward the initial value, reaching saturation at around 20 T. One can understand the experimental behavior of the strain (Figure 1c) at low temperature assuming that B^1_{10} and B^1_{11} are both positive, and B^1_{10} is a few times larger than B^1_{11}. Then, the increase of the expectation value of the $Q_{x^2-y^2}$ quadrupolar leads to a contraction, whereas the initial decrease of the expectation value of Q_{3z^2} results in an expansion along the *b*-axis. In low fields the *b*-axis steadily expands since $B^1_{10} > B^1_{11}$, but at around 10 T, the steady growth is replaced by a very fast contraction with increasing applied field, since the Q_{3z^2} quadrupolar starts increasing. This explains the shape of the experimental curve (steady elongation followed by sharp contraction) in Figure 2a at low temperature, and the saturation above 20 T.

To illustrate this, we have used the ab initio calculated $\langle Q_{3z^2} \rangle$ and $\langle Q_{x^2-y^2} \rangle$ and the phenomenological fitting parameters ($\frac{B^1_{11}}{B^1_{10}} = 2.0 \times 10^{-2}$ and $\frac{B^1_{10}}{K} = 5.85 \times 10^{-5}$), to compare the theory (Equation (7)) with the experiment. Our estimation for the magnetoelastic constant $\frac{B^1_{10}}{K} = 5.85 \times 10^{-5}$ together with the $C_{bb} = 41$ GPa[43] corresponds to $B^1_{10}/\alpha_J \approx 1.1 \times 10^4$ K, (where $\alpha_J \equiv \Theta_2$ is the Stevens factor) are in good agreement with measured values of the order 10^4 K reported for similar rare-earth-based oxides.[44] The comparison is presented in Figure 3b. Taking into account the approximation we made, the agreement is quite fair.

Thus, from the ab initio calculated quadrupolar moments, one can understand and describe the behavior of the strain in applied magnetic field, and even quantitatively predict the field range at which elongation turns into contraction. A more refined numerical theory of the effect would, however, require a consideration of the full magnetoelastic and elastic Hamiltonians with a whole set of unknown elastic and magnetoelastic constants from Equations (3) and (5). In addition, one needs to account for possible corrections to the linear theory due to high-field-induced changes in the local symmetry of the Er^{3+} ion environment, which are currently unknown.

3. Conclusion and Outlook

To conclude, we found that $KEr(MoO_4)_2$ exhibits massive magnetostriction induced by the single-ion effect, which becomes most prominent below 20 K. Through a variety of experimental techniques and state-of-the-art first-principle many-body theory calculations, we have shown on a microscopic level how the magnetic field induces a lattice distortion in $KEr(MoO_4)_2$ due to the change of the erbium quadrupolar moments. Our study uncovers the single-ion mechanism for the magnetostriction in magnetically disordered rare-earth compounds and offers a new approach to investigate these peculiar materials.

The extremely high sensitivity to the magnetic field variation in the vicinity of the critical field $\mu_0 H_{cr}$ together with a giant magnetocaloric effect reported earlier on this compound[9] $KEr(MoO_4)_2$ provides great perspectives for applications in cryogenic and magnetic technologies.

4. Computational Methodology

Our charge self-consistent DFT+DMFT calculations in conjunction with the HI approximation, abbreviated below as DFT+HI, were carried out for the high-temperature orthorombic structure of $KEr(MoO_4)_2$ with the lattice parameters $a = 5.06$, $b = 18.23$, and $c = 7.92$ Å. The corresponding unit cell volume per formula unit is $V_0 = 182.6$ Å^3. We employed the Wien-2k full-potential code[45] in conjunction with "TRIQS" library implementations for the DMFT cycle[46,47] and HI. The spin-orbit coupling was included in Wien2k within the standard second-variation treatment. The Brillouin zone (BZ) integration was carried out using 60 **k**-points in the full BZ and the local density approximation

(LDA) was employed as DFT exchange-correlation potential. The Wannier orbitals representing Er 4*f* states were constructed by the projective technique of ref. [48,49] using the Kohn–Sham bands enclosed by the energy window [−2.72:1.36] eV around the Kohn–Sham Fermi energy; this window thus encloses all Er 4*f*-like bands. The on-site Coulomb interaction between Er 4*f* was specified by the Slater parameter $F_0 = 7$ eV and the Hund's rule coupling $J_H = 1.01$ eV. The double-counting correction was computed using the fully localized limit (FLL)[50] with the atomic occupancy of the Er f^{11} shell.[51] The DFT+DMFT charge self-consistency was implemented as described in ref. [52]. In our self-consistent DFT+HI calculations, we employed the spherical averaging of the Er 4*f* charge density, following the approach of Delange et al.[38] in order to suppress the contribution of LDA self-interaction error to the crystal field; this approach was previously shown to be reliable for quantitative evaluation of CEF splitting on 4*f* ions.[38,53] The DFT+HI calculations were converged to 0.1 mRy in the total energy.

5. Experimental Section

Single crystal samples of $KEr(MoO_4)_2$ were grown from a melt by slow cooling at ILTPE (Kharkiv, Ukraine). The correct elemental composition as well as the homogeneity of samples used for this study are characterized by energy-dispersive X-ray spectroscopy. The measurements of the crystallographic structure and the orientation of the sample has been done using Laue X-ray diffraction method. The samples for magnetization and magnetostriction measurements were cleaved from the same bulk crystal. Measurements were performed with three different experimental techniques in order to explore the magnetic field effect on $KEr(MoO_4)_2$. A high-resolution capacitance dilatometer was used for the magnetostriction experiment.[29] The size of the sample was $4 \times 4 \times 0.062$ mm^3. The magnetization was measured by VSM[31] on the sample with mass $m = 6.2$ mg. Using literature data of low field magnetization,[28] the curve obtained by the VSM was scaled to get the physical μ_B/Er^{3+} unit. In both experiments, the magnetic field and the *b*-axis of the crystal were parallel to the shortest side of the plate-shaped sample.

Supporting Information

Supporting Information is available from the Wiley Online Library or from the author.

Acknowledgements

This work was supported by HFML-RU, member of the European Magnetic Field Laboratory (EMFL). This work is part of the research program of the Netherlands Organisation for Scientific Research (NWO). The authors also thank Nigel E. Hussey for useful discussions, Uli Zeitler for technical help during the VSM experiment, and Lilian Prodan for assistence with energy-dispersive X-ray spectroscopy. D.K. was supported by the PRIME program of the German Academic Exchange Service (DAAD) with funds from the German Federal Ministry of Education and Research (BMBF). L.V.P. acknowledges support by the European Research Council grant ERC-319286-"QMAC" and the computer team at CPHT.

Open access funding enabled and organized by Projekt DEAL.

Conflict of Interest

The authors declare no conflict of interest.

Data Availability Statement

The data that support the findings of this study are available from the corresponding author upon reasonable request.

Keywords

density-functional theory, magnetostriction, rare-earth magnetism

Received: July 28, 2021
Revised: November 4, 2021
Published online:

[1] T. Gottschall, E. Bykov, A. Gràcia-Condal, B. Beckmann, A. Taubel, L. Pfeuffer, O. Gutfleisch, L. Mañosa, A. Planes, Y. Skourski, J. Wosnitza, *J. Appl. Phys.* **2020**, *127*, 185107.
[2] K. Dey, S. Sauerland, J. Werner, Y. Skourski, M. Abdel-Hafiez, R. Bag, S. Singh, R. Klingeler, *Phys. Rev. B* **2020**, *101*, 195122.
[3] A. Miyata, H. Suwa, T. Nomura, L. Prodan, V. Felea, Y. Skourski, J. Deisenhofer, H.-A. K. von Nidda, O. Portugall, S. Zherlitsyn, V. Tsurkan, J. Wosnitza, A. Loidl, *Phys. Rev. B* **2020**, *101*, 054432.
[4] T. D. Lacheisserie, E. Du, *Magnetostriction: Theory and Applications of Magnetoelasticity*, CRC Press, Boca Raton, FL **1993**.
[5] J. J. Rhyne, S. Legvold, *Phys. Rev.* **1965**, *138*, A507.
[6] A. E. Clark, H. S. Belson, N. Tamagawa, *AIP Conf. Proc.* **1973**, *10*, 749.
[7] S. Buck, M. Fähnle, *Phys. Rev. B* **1998**, *57*, R14044.
[8] M. Doerr, M. Rotter, A. Lindbaum, *Adv. Phys.* **2005**, *54*, 1.
[9] V. Tkáč, A. Orenáčová E. Čižmár, M. Orendáč, A. Feher, A. G. Anders, *Phys. Rev. B* **2015**, *92*, 024406.
[10] L. Weymann, L. Bergen, T. Kain, A. Pimenov, A. Shuvaev, E. Constable, D. Szaller, B. V. Mill, A. M. Kuzmenko, V. Y. Ivanov, N. V. Kostyuchenko, A. I. Popov, A. K. Zvezdin, A. Pimenov, A. A. Mukhin, M. Mostovoy, *npj Quantum Mater.* **2020**, *5*, 61.
[11] D. I. Abubakirov, K. Matsumoto, H. Suzuki, M. S. Tagirov, *J. Phys.: Condens. Matter* **2008**, *20*, 395223.
[12] N. F. Vedernikov, A. K. Zvezdin, Z. Levitin, A. I. Popov, *J. Exp. Theor. Phys.* **1988**, *67*, 358.
[13] P. Morin, J. Rouchy, Z. Kazei, *Phys. Rev. B* **1995**, *51*, 15103.
[14] C. Detlefs, F. Duc, Z. A. Kazeĭ, J. Vanacken, P. Frings, W. Bras, J. E. Lorenzo, P. C. Canfield, G. L. J. A. Rikken, *Phys. Rev. Lett.* **2008**, *100*, 056405.
[15] L. A. Bumagina, V. I. Krotov, B. Z. Malkin, A. K. Khasanov, *J. Exp. Theor. Phys.* **1981**, *53*, 792.
[16] Y. He, X. Ke, C. Jiang, N. Miao, H. Wang, J. M. D. Coey, Y. Wang, H. Xu, *Adv. Funct. Mater.* **2018**, *28*, 1800858, _eprint: https://onlinelibrary.wiley.com/doi/pdf/10.1002/adfm.201800858.
[17] J. Jensen, A. R. Mackintosh, *Rare Earth Magnetism: Structures and Excitations*, International Series of Monographs on Physics. Oxford University Press, Oxford **1991**.
[18] S. Sachdev, *Nat. Phys.* **2008**, *4*, 173.
[19] S. T. Bramwell, M. J. P. Gingras, *Science* **2001**, *294*, 1495.
[20] A. Anders, S. Volotskii, O. Zubkov, *Low Temp. Phys.* **1994**, *20*, 105.
[21] A. A. Zvyagin, K. Kutko, D. Kamenskyi, A. V. Peschanskii, S. Poperezhai, N. M. Nesterenko, *Phys. Rev. B* **2018**, *98*, 064406.
[22] A. Orendáčová, D. Horváth, M. Orendáč, E. Čižmár, M. Kačmár, V. Bondarenko, A. G. Anders, A. Feher, *Phys. Rev. B* **2001**, *65*, 014420.
[23] G. A. Gehring, K. A. Gehring, *Rep. Prog. Phys.* **1975**, *38*, 1.
[24] G. Bogomolova, A. Kaminskii, P. Klevtsov, A. Kuznetsov, L. Li, A. Pavluk, *Optica i spectroskopija* **1971**, *31*, 259.
[25] V. I. Kut'ko, *Low Temp. Phys.* **2005**, *31*, 1.
[26] B. M. Wanklyn, F. R. Wondre, *J. Cryst. Growth* **1978**, *43*, 93.

[27] E. Khatsko, A. Cherny, A. Kaplienko, *Low Temp. Phys.* **1993**, *19*, 864.
[28] S. Mat'aš, E. Dudzik, R. Feyerherm, S. Gerischer, S. Klemke, K. Prokeš, A. Orendáčová, *Phys. Rev. B* **2010**, *82*, 184427.
[29] R. Küchler, T. Bauer, M. Brando, F. Steglich, *Rev. Sci. Instrum.* **2012**, *83*, 095102.
[30] P. Morin, Z. Kazei, *Phys. Rev. B* **1997**, *55*, 148887.
[31] A. Sazonov, V. Hutanu, M. Meven, G. Roth, H. Murakawa, Y. Tokura, V. K. Guduru, L. C. J. M. Peters, U. Zeitler, L. F. Kiss, D. Szaller, B. Náfrádi, I. Kézsmárki, *Phys. Rev. B* **2017**, *95*, 174431.
[32] F. Mouhat, F.-X. Coudert, *Phys. Rev. B* **2014**, *90*, 224104.
[33] A. M. Kadomtseva, I. B. Krynetsky, M. D. Kuz'min, A. K. Zvezdin, *J. Magn. Magn. Mater.* **1989**, *81*, 196.
[34] P. Morin, J. Rouchy, E. du Tremolet de Lacheisserie, *Phys. Rev. B* **1977**, *16*, 3182.
[35] A. Abragam, B. Bleaney, *Electron Paramagnetic Resonance of Transition Ions*, Oxford Classic Texts in the Physical Sciences, Oxford University Press, Oxford **2012**.
[36] S. Poperezhai, P. Gogoi, N. Zubenko, K. Kutko, V. I. Kutko, A. S. Kovalev, D. Kamenskyi, *J. Phys.: Condens. Matter* **2017**, *29*, 095402.
[37] K. W. H. Stevens, *Proc. Phys. Soc. A* **1952**, *65*, 209.
[38] P. Delange, S. Biermann, T. Miyake, L. Pourovskii, *Phys. Rev. B* **2017**, *96*, 155132.
[39] A. Georges, G. Kotliar, W. Krauth, M. J. Rozenberg, *Rev. Mod. Phys.* **1996**, *68*, 13.
[40] V. I. Anisimov, A. I. Poteryaev, M. A. Korotin, A. O. Anokhin, G. Kotliar, *J. Phys.: Condens. Matter* **1997**, *9*, 7359.
[41] J. Hubbard, B. H. Flowers, *Proc. R. Soc. London, Ser. A* **1963**, *276*, 238.
[42] $KEr(MoO_4)_2$ ($KEr[MoO_4]_2$ rt) Crystal Structure - SpringerMaterials, https://materials.springer.com/isp/crystallographic/docs/sd_0377911.
[43] G. A. Zvyagina, A. A. Zvyagin, *Low Temp. Phys.* **2000**, *26*, 354.
[44] P. Morin, Z. Kazei, *J. Phys.: Condens. Matter* **1999**, *11*, 1289.
[45] P. Blaha, K. Schwarz, G. K. H. Madsen, D. Kvasnicka, J. Luitz, R. Laskowsk, F. Tran, L. Marks, L. Marks, *WIEN2k: An Augmented Plane Wave Plus Local Orbitals Program for Calculating Crystal Properties*, Karlheinz Schwarz, Vienna University of Technology, Austria **2018**.
[46] M. Aichhorn, L. Pourovskii, P. Seth, V. Vildosola, M. Zingl, O. E. Peil, X. Deng, J. Mravlje, G. J. Kraberger, C. Martins, M. Ferrero, O. Parcollet, *Comput. Phys. Commun.* **2016**, *204*, 200.
[47] O. Parcollet, M. Ferrero, T. Ayral, H. Hafermann, I. Krivenko, L. Messio, P. Seth, *Comput. Phys. Commun.* **2015**, *196*, 398.
[48] B. Amadon, F. Lechermann, A. Georges, F. Jollet, T. O. Wehling, A. I. Lichtenstein, *Phys. Rev. B* **2008**, *77*, 205112.
[49] M. Aichhorn, L. Pourovskii, V. Vildosola, M. Ferrero, O. Parcollet, T. Miyake, A. Georges, S. Biermann, *Phys. Rev. B* **2009**, *80*, 085101.
[50] M. T. Czyżyk, G. A. Sawatzky, *Phys. Rev. B* **1994**, *49*, 14211.
[51] L. V. Pourovskii, B. Amadon, S. Biermann, A. Georges, *Phys. Rev. B* **2007**, *76*, 235101.
[52] M. Aichhorn, L. Pourovskii, A. Georges, *Phys. Rev. B* **2011**, *84*, 054529.
[53] L. V. Pourovskii, J. Boust, R. Ballou, G. G. Eslava, D. Givord, *Phys. Rev. B* **2020**, *101*, 214433.